
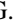
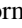




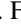
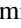


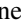



Ramp compression of tantalum to multiterapascal pressures: Constraints of the thermal equation of state to 2.3 TPa and 5000 K

M. G. Gorman ^{*}, C. J. Wu [†], R. F. Smith, L. X. Benedict, C. J. Prisbrey , W. Schill, S. A. Bonev, Z. C. Long , P. Söderlind , D. Braun, D. C. Swift, R. Briggs , T. J. Volz , E. F. O'Bannon , P. M. Celliers , D. E. Fratanduono, J. H. Eggert , S. J. Ali , and J. M. McNaney 

Lawrence Livermore National Laboratory, 7000 East Avenue, Livermore, California 94500, USA

 (Received 14 October 2022; revised 5 January 2023; accepted 11 January 2023; published 27 January 2023)

We report measurements of the compressibility of ramp compressed tantalum to a final stress of 2.3 TPa corresponding to threefold volumetric compression. Using these data, we extended the experimental constraint on the Ta cold compression curve by an order of magnitude in pressure. By combining the resulting data with previous measurements of shock compression and ambient pressure heating, we construct an experimentally bounded and thermodynamically consistent equation of state model for Ta which has 2% uncertainty in pressure at 1 TPa. We therefore propose Ta as an *in situ* pressure scale for laser-heated static compression experiments which were recently able to reach terapascal pressures and thousands of degrees Kelvin. Our new equation of state of Ta is experimentally constrained at extreme pressures and temperatures relevant to a wide range of planetary interiors and will allow for more accurate comparison between experimental measurements and theory at extreme conditions.

DOI: [10.1103/PhysRevB.107.014109](https://doi.org/10.1103/PhysRevB.107.014109)

I. INTRODUCTION

Extreme pressures and temperatures can dramatically change the structure, bonding, and mechanical properties of materials. Indeed, coupling the laser-heated diamond anvil cell (DAC) with *in situ* x-ray diffraction techniques led to numerous important discoveries ranging from novel material syntheses [1,2] to understanding material properties at planetary interior conditions above 100 GPa [3]. The recent coupling of laser heating techniques with double-stage (DS-DAC) and toroidal diamond anvil cells [4], where the sample is compressed statically between two opposing diamonds with culet sizes of ~ 20 μm , now facilitates the study of novel material behavior above 1 TPa (1 TPa = 10 million atm) and several thousand degrees Kelvin. However, a key challenge of such experiments is accurately determining the sample pressure at elevated temperatures due to the lack of an experimentally benchmarked high-temperature pressure standard. In addition, noble metals have often been chosen as pressure standards for room temperature static compression studies due to their high x-ray scattering efficiency, simple crystal structure, and phase stability up to extreme pressures. However, some have recently been shown to undergo structural phase transformations at high temperature [5–9] and so may not be suitable as standards at elevated temperatures. This means that new candidate materials may be necessary for thermal pressure standards at terapascal conditions.

Shock compression experiments, where the sample is compressed discontinuously, can be used to provide absolute

measurements of stress and density along a path known as the Hugoniot (purple curve in Fig. 1). However, such compression also generates significant heating, which means that the study of solid matter is precluded for most materials above 0.2–0.3 TPa. Conversely, laser-driven ramp compression provides an avenue for high-pressure, low-temperature studies, meaning that sample materials can remain in the solid phase at extreme pressures and densities. The sample follows a compression path close to the principal isentrope (blue curve in Fig. 1). This technique was used recently to establish high-accuracy pressure benchmarks for Cu, Au, and Pt to beyond 1 TPa at room temperature [16,17]. However, such measurements do little to bound the thermal components of the equation of state (EOS), meaning that considerable uncertainty still exists in the pressure P -density ρ relation as a function of temperature T . By combining experimental measurements which sample different thermodynamic compression paths, the opportunity exists to develop an experimentally bounded EOS which is valid to extreme densities and high temperatures relevant for double-stage DAC experiments.

Tantalum is a material that exhibits remarkable phase stability up to extreme pressures and temperatures [18,19], has a bcc crystal structure, and has high x-ray scattering efficiency. In this work, we present ramp compression measurements of Ta up to 2.3 TPa and 53.0 g/cm³, representing threefold volumetric compression. These measurements extend the experimental constraints on the Ta cold curve by an order of magnitude in pressure, which, taken together with previous experimental measurements under shock compression [19–25] and isobaric heating [26], allows for the construction of an experimentally benchmarked high-temperature EOS of Ta at terapascal pressures. This model, which has uncertainties

^{*}Corresponding author: gorman11@llnl.gov

[†]Corresponding author: wu5@llnl.gov

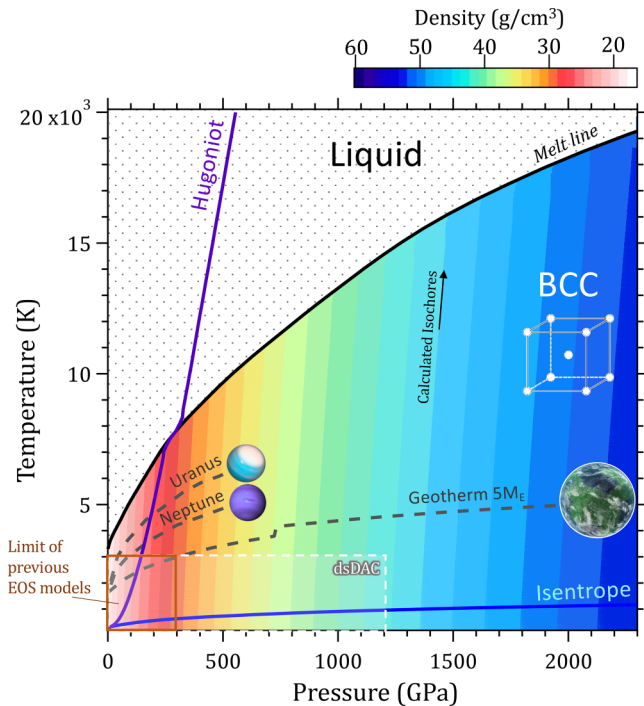


FIG. 1. The temperature-pressure phase diagram of Ta. Recent advances in static compression have enabled the study of matter beyond 1 TPa at elevated temperatures (white dashed box). Laser-driven ramp compression allows materials to be studied in their solid form to extreme pressures close to an isentrope (blue line). Shock compression achieves states along a thermodynamic path called the Hugoniot (purple line). The ramp compression measurements presented here, in addition to previous experimental data sets, allow for the construction of an accurate high-temperature Ta EOS far beyond the conditions constrained previously [10–13] (orange box). Temperature-pressure conditions similar to those found in planetary interiors are now within the operating limits of our EOS (gray dashed lines) [14,15]. The melt curve, density color map, and isochores are outputs of our high-temperature EOS.

of 2% at pressures of 1 TPa, will serve as an accurate high-temperature pressure standard for use in static compression experiments.

EOS models consist of cold (T -independent) contributions and thermal pieces (accounting for ionic and electronic excitations). Prior to the advent of high-pressure ramp compression data, EOS models were constrained by fitting the cold contribution to DAC data, the low-pressure part of the thermal terms to thermal expansion (obtained from both ambient heating and high-pressure, high-temperature DAC experiments) and specific heat measurements, and the high-pressure thermal terms to shock Hugoniot data. However, there is a problem with this strategy: It is generally not the case that DAC and shock data exist over the *same* range of ρ for any material. Thus, when a wide-range EOS model is desired, one is forced to extrapolate the DAC-derived $P_{\text{cold}}(\rho)$ to values of ρ beyond the static high- P data themselves, so that the difference with the shock data can be used to extract the thermal component. This leads to uncertainties in the EOS which grow with both P and T , as discussed in Ref. [27]. The addition of ramp compression overcomes this difficulty by augmenting the DAC-derived

$P_{\text{cold}}(\rho)$ at low ρ with additional $P(\rho)$ data at higher ρ , into (and even well beyond) the compression regime of single- and double-shock data. These data lie close to an isentrope and are therefore at significantly lower T than that of the shock Hugoniot, as illustrated for Ta in Fig. 1. An added benefit is that this locus of states samples solid-state compression and is closer in T to the interior conditions of planets, leading to an EOS model which is better constrained for these astrophysical applications.

In this work, we use our Ta ramp compression measurements together with existing isobaric and shock wave data to make an accurate EOS model for Ta without appealing to high- ρ extrapolations of $P_{\text{cold}}(\rho)$. In so doing, we provide the high-pressure science community with a more accurate standard for the determination of pressure at large compressions and temperatures.

II. RAMP COMPRESSION OF TANTALUM USING LASERS

To directly constrain the cold curve up to multiterapascal pressures, we ramp compressed Ta using the National Ignition Facility (NIF). The experimental and analysis techniques used in this work have been described elsewhere [14,16,17] and are summarized here (for more information, see the Supplemental Material [28] and Refs. [29–40] therein). We used up to 1.5 MJ of laser energy in 168 beams at NIF in a 30 ns pulse to ramp compress Ta samples up to a peak pressure of 2.30 TPa. Laser intensity was incident on a gold hohlraum, generating an x-ray bath which directly ablated the target package mounted on an opening on its side [Fig. 2(a)]. The target package consists of a Cu ablator and a four-step Ta brick [Fig. 2(a)]. The ablation drive imparted an initial low-pressure (76–117 GPa) steady shock on the Ta sample, followed by a monotonically increasing ramp pressure wave. The gradual nature of the compression ensures the Ta sample follows a much cooler thermodynamic path relative to the Hugoniot and thus remains in the solid phase up to extreme pressures (see Fig. 1) [16]. The Ta sample consisted of four steps of thicknesses of approximately 91, 96, 101, and 106 μm [Fig. 2(a)] and a width of 200 μm . A velocity interferometer system for any reflector (VISAR) [42] was used to measure the free surface velocity history $U_{\text{FS}}(t)$ for each thickness [Fig. 2(a)] during compression. The multistep nature of the target is key, as the difference in wave arrival times at two different sample depths allows for the absolute determination of the Lagrangian sound speed as a function of particle velocity $C_L(u_p)$ [43]. By integrating $C_L(u_p)$, we can extract the longitudinal stress-density relation and the associated uncertainties along a ramp compression path. Crucially, unlike EOS experiments performed in a DAC, the data here do not rely on a standard to determine the stress-density relationship.

The region of $C_L(u_p)$ below the initial shock state is obtained using an EOS model for Ta [44] which is assumed to correctly describe the isentropic release down to zero pressure. C_L and its uncertainty $\sigma_{C_L}(u_p)$ were obtained from thickness and velocity versus time data by linear regression using errors determined by our measurement accuracies. Figure 2(b) shows the Lagrangian sound speed versus particle velocity for seven NIF experiments on Ta along with 1σ uncertainties and the weighted average of these experiments.

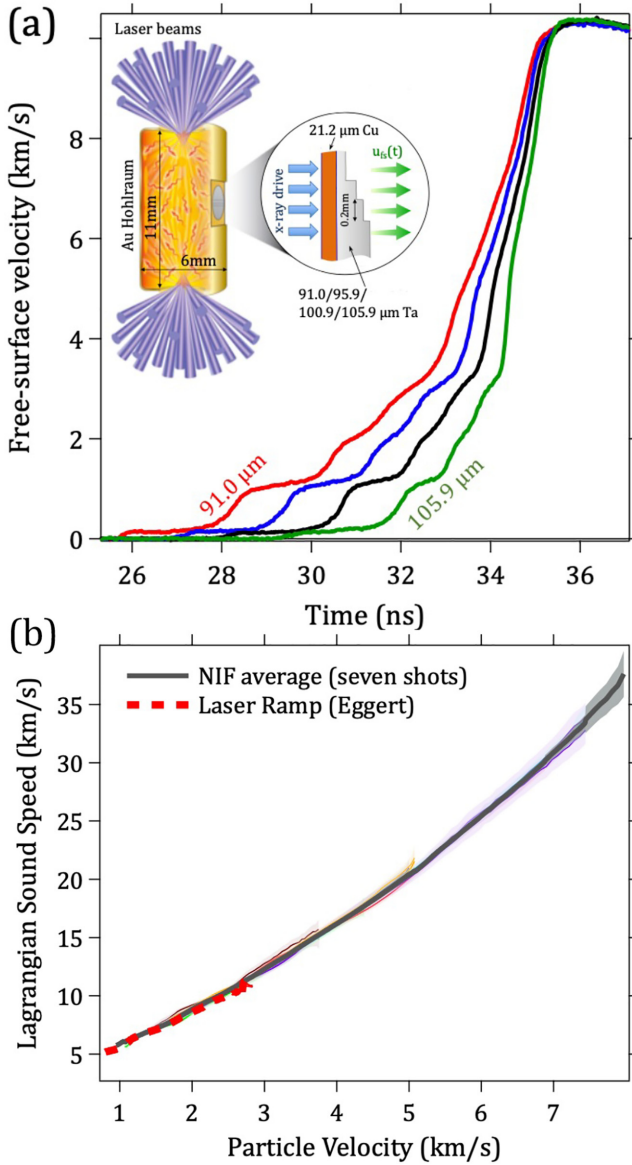


FIG. 2. (a) A temporally shaped laser pulse irradiates an Au hohlraum which generates an x-ray bath and launches a gradual compression wave into the stepped Ta sample. A spatially resolving VISAR records the free surface velocity history from each of the four steps (colored traces). (b) Ta Lagrangian sound speed versus particle velocity for seven NIF experiments on Ta is shown with 1σ uncertainties. The averaged stress-density response is shown in black. Data from previous laser experiments are shown for comparison [41].

Our data are in excellent agreement with previous laser-driven ramp compression experiments on Ta [41]. $C_L(u_p)$ and $\sigma_{C_L}(u_p)$ are integrated to obtain

$$P_x = P_H + \rho_0 \left[\int_{u_{p,H}}^{u_p} C_L, du_p \right] \quad (1)$$

and

$$\rho = \left([1/\rho_H] - [1/\rho_0] \times \left[\int_{u_{p,H}}^{u_p} du_p / C_L \right] \right)^{-1} \quad (2)$$

and their uncertainties

$$\sigma_{P_x}^2 = \sigma_{P_{x,H}}^2 + \rho_0 \left[\int_{u_{p,H}}^{u_p} \sigma_{C_L} du_p \right] \quad (3)$$

and

$$\sigma_\rho^2 = \left([\rho_H^2 / \rho_0^2] (\delta\rho_H)^2 + \left([\rho^2 / \rho_0] \times \left[\int_{u_{p,H}}^{u_p} [\sigma_{C_L} / C_L^2] du_p \right] \right)^2 \right). \quad (4)$$

Here, P_H , ρ_H , and $u_{p,H}$ are the pressure, density, and particle velocity, respectively, associated with the initial shock Hugoniot state. Uncertainties are propagated through the integrals linearly, rather than in quadrature, because they appear to be strongly correlated rather than random. This method of uncertainty propagation allows for the direct propagation of experimental uncertainties.

We make several corrections to reduce the measured longitudinal stress σ_x to the isentropic pressure P_{isen} . First, the thermal pressure associated with the initial shock state is accounted for, reducing the stress density along the shock-ramp path to a shockless stress-density path. The temperature at the initial shock state is estimated by using a previous tabular EOS of Ta [44], and the thermal pressure difference is approximated as $P_{\text{shock-ramp}} - P_{\text{shockless}} = \gamma \rho [E_{\text{th}}(T_{\text{shock-ramp}}) - E_{\text{th}}(T_s)]$, where E_{th} is the thermal energy at density ρ and temperature $T_{\text{shock-ramp}}$ along the shock-ramp path or temperature T_s along the shockless compression path as determined from the Debye integral and γ is the Grüneisen parameter. The temperature along the shock-ramp path is determined from integrating the thermodynamic derivative $\gamma \frac{\partial \ln T_x}{\partial \ln \rho}$ [45]. To relate the measured longitudinal stress to an equivalent hydrostatic pressure we assume the von Mises criterion: $\sigma_x = P_{\text{hyd}} + 2/3Y(P)$, where Y is the yield strength. If a solid supports strength at high pressure, the thermal pressure from plastic work heating must also be accounted for. Plastic work heating causes the pressure on the hydrostat to deviate from the isentrope by $P_{\text{hyd}} - P_{\text{isen}} = \gamma \rho \int_0^{\epsilon_x} \beta dW_p$, where ϵ_x is the natural strain $\log(\rho/\rho_0)$ and β is the Taylor-Quinney factor, which describes the fraction of plastic work that partitions into the thermal energy of the system. Here, β is assumed to equal 1, which assumes all plastic work is used to heat the material [46]. dW_p is the plastic work heating. To make these corrections and reduce our measurements of longitudinal stress to isentropic pressure, we require a model for the Grüneisen parameter $\gamma(P)$, the plastic work heating dW_p , and the yield strength Y_p (see Supplemental Material, Sec. C [28]). Figure 3 shows the percentage correction as a function of stress for the deviatoric stress, plastic work heating, and initial shock heating terms. The magnitude of the total correction when reducing our ramp path to the principal isentrope is $\sim 4\%$ at 2.3 TPa (black curve in Fig. 3). To determine the pressure along the 298 K isotherm or cold curve, one must subtract the thermal pressure from the isentrope at the elevated temperature along the isentrope T_s . For example, the pressure along the 298 K isotherm, $P_{298\text{K}} = P_s - \gamma \rho [E_{\text{th}}(T_s) - E_{\text{th}}(298\text{K})]$, where E_{th} is the thermal energy at density ρ determined from the Debye integral. The thermal pressure difference between

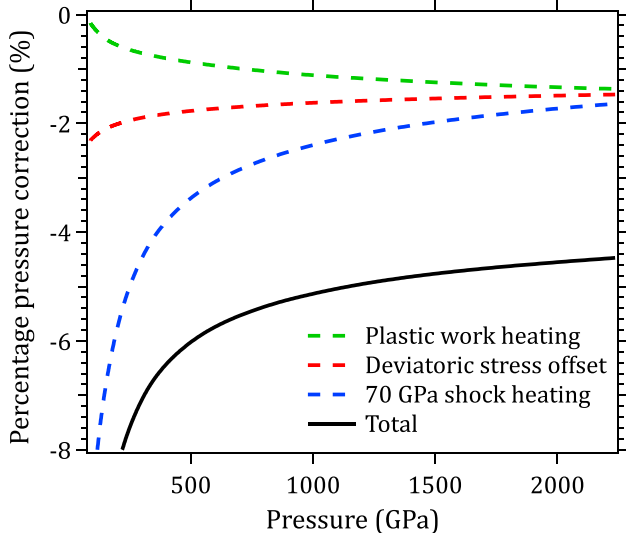


FIG. 3. The percent correction applied to reduce the measured stress-density response to a hydrostatic pressure-density isentrope. The total correction is $\sim 4\%$ at 2.3 TPa.

the isentrope and 298 K isotherm is calculated to be very small (~ 5 GPa) at 2 TPa.

Figure 4 shows the determined stress-density relationship of Ta up to 2.3 TPa, which was averaged from seven NIF experiments (black dashed line; see Fig. S2 for data from individual experiments) and the resulting 298 K isotherm (solid black line) [28]. The experimental uncertainties from stress and density are combined into a standard uncertainty in stress calculated from

$$\delta\sigma_x(\rho) = \sqrt{\delta\sigma_x(u_p)^2 + \left(\frac{\partial\sigma_x}{\partial\rho}\delta\rho(u_p)\right)^2}. \quad (5)$$

It is likely that combining the uncertainties in this manner represents an overestimate of the total uncertainty as Eq. (5) assumes that the uncertainties in stress and density are uncorrelated. The 1σ uncertainty in pressure of our Ta isotherm at 1 TPa is 2%, demonstrating unprecedented precision at pressure conditions around 3 times Earth's core. Our data are in agreement with both previous shockless compression experiments performed using laser [41] (red line) and pulsed power [47,48] (purple line) and previous isotherms determined from static compression experiments (colored symbols). A comparison with previous room temperature Ta isotherms from DACs, reduced shock waves, and ultrasonic data is shown in the inset of Fig. 4. Our 298 K isotherm shows excellent agreement with isotherms from hydrostatic DAC experiments [51,52,55] up to pressures where they are constrained by data. Cynn and Yoo [51] used an Au pressure standard in their study and used an Au EOS from Heinz and Jeanloz [56] to determine the Ta sample pressure. Interestingly, the Ta pressures determined using the Heinz and Jeanloz EOS are systematically lower than the isotherm determined from this work (see Fig. S7 [28]). However, by reinterpreting the Cynn and Yoo data using an updated Au pressure standard recently established from ramp compression [17], we find the agreement between the Ta compression data of Cynn and Yoo and this work im-

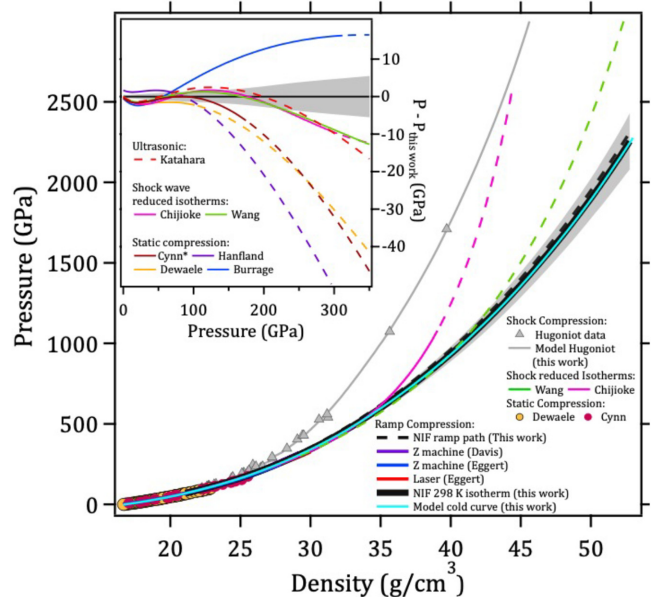


FIG. 4. The pressure-density response of Ta to pressures up to 2.3 TPa and 53 g/cm^3 . The measured stress (black dashed line) and 298 K isotherm (black line) are shown. The error bars represent 1σ standard deviation of multiple measurements collected and averaged into a single result, which also includes measurement uncertainties. Previous ramp compression data from pulsed power [47,48] (blue and purple) and laser [41] (red) experiments and shock wave reduced isotherms [49,50] (pink and green) are shown as colored lines. Shock wave [20–25] (gray symbols) and static [51,52] (red and orange symbols) data are shown for comparison. The computed cold curve and Hugoniot of the new EOS are shown by cyan and gray curves, respectively. Inset: Comparison of room temperature isotherms from previous studies [49–55] and the 298 K isotherm determined in this work. Solid lines denote the regions where the isotherms are constrained by data, and dashed lines indicate extrapolations. The asterisk indicates that the data of Cynn have been reinterpreted using a different EOS of Au [17] (see main text).

proves considerably (maroon curve in the inset of Fig. 4). The isotherm of Ref. [53], which was determined from data which extended up to 0.31 TPa, is stiffer than our 298 K isotherm, most likely due to the nonhydrostatic conditions in which the Ta samples were compressed in those experiments as no pressure-transmitting medium was used. Our 298 K isotherm is key to the construction of an accurate high- T EOS of Ta as it bounds $P_{\text{cold}}(\rho)$ up to 2.3 TPa, which is the dominant contribution to the total material response at terapascal pressures and temperatures of several thousand degrees Kelvin.

III. CONSTRAINING OUR TANTALUM EQUATION OF STATE MODEL

We now describe the construction of a Ta EOS model which uses our ramp compression measurements as a primary constraint. As described above, this fixes $P_{\text{cold}}(\rho)$ up to 2.3 TPa. To further constrain the EOS of Ta at elevated temperature, we utilize a wealth of existing experimental data. The key constraints for the thermal component of the EOS include (1) thermodynamic data (T -dependent density, entropy,

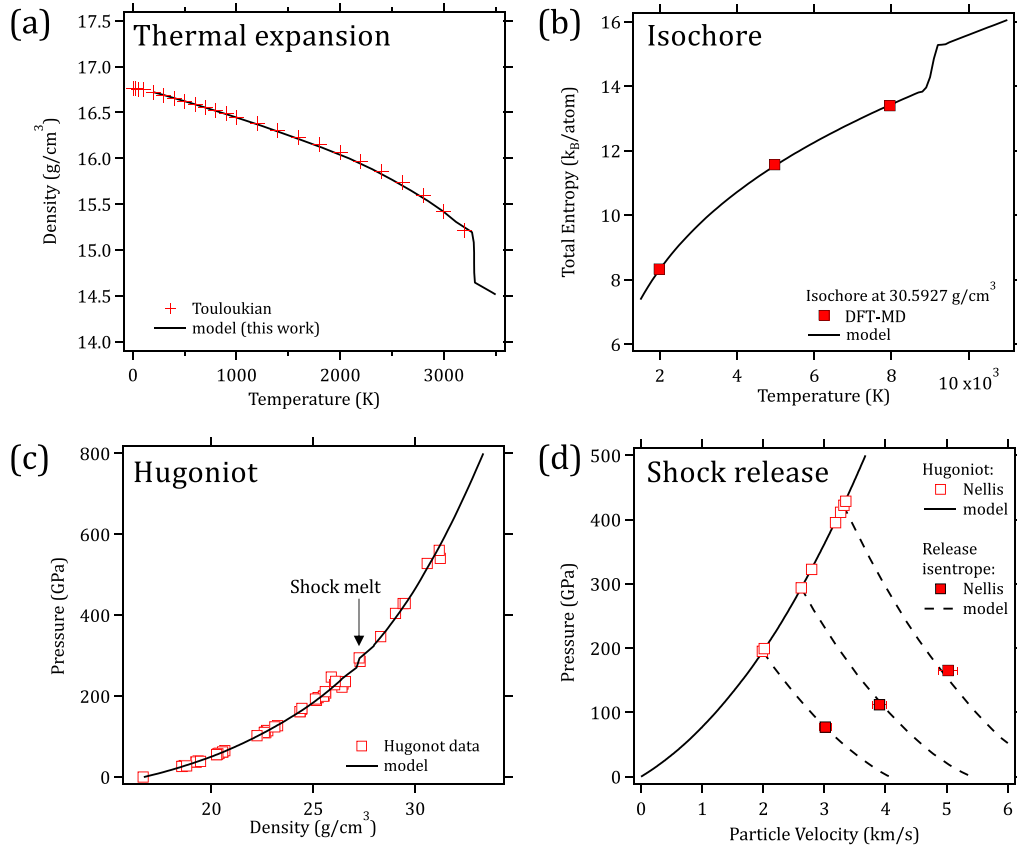


FIG. 5. Comparison of high-temperature experimental and theory data for Ta with our EOS model. (a) Ambient pressure heating data from Touloukian *et al.* [62]. (b) A 30.5927 g/cm³ isochore determined from DFT-based molecular dynamics simulations. (c) Shock Hugoniot data obtained with two-stage gas gun and convergent explosive drive experiments. [20–25] (d) Shock release data from two-stage gas gun experiments [63]. The parameters of our high-temperature EOS model are varied until excellent agreement is found with these data (see text).

and enthalpy) near ambient pressure; (2) melt temperatures $T_{\text{melt}}(P)$ at both ambient and elevated pressures as measured in laser-heated DACs below 100 GPa and informed by the shock melting study of Kraus *et al.* at several hundred gigapascals [19]; (3) density functional theory (DFT) based molecular dynamics predictions of isochores of internal energy, pressure, and entropy, which were used to supplement experimental constraints in regions inaccessible by experiment; and (4) shock Hugoniot data [20–25] used to constrain thermal pressure $P_{\text{thermal}}(\rho, E)$ as a function of density and internal energy (see Figs. 5 and S9–S13). These experimental shock data were extended up to pressures of ~ 2.5 TPa and were collected using two-stage gas guns and convergent explosive drives. Regarding $T_{\text{melt}}(P)$, it is noteworthy that when fitting to the DAC melting data of Dewaele *et al.* [52], we made use of their measured $T_{\text{melt}} vs \rho$ relationship; $T_{\text{melt}}(P)$ was then determined from our EOS model (see Fig. S12 [28]).

Importantly, recent measurements of the shock melting pressure [19] provide an additional connection between this E -dependent function and the temperature. We use previous isobaric heating data to constrain the specific heat C_V [26] and previous ambient pressure melting data to constrain the entropy of melting [38] (Fig. S9 [28]). We employ various models to capture the complete EOS behavior of Ta, which will be discussed in more detail below. The parameters of each

model are varied in concert until satisfactory agreement with all experimental data is obtained. We utilized the multiphase equation of state generation code [57], developed at Lawrence Livermore National Laboratory, to aid in this iterative fitting process.

A. Model forms

The models we use for the cold and thermal terms of the free energy are the same as those employed in Ref. [57]. We take the Helmholtz free energy, $F = E - TS$ (where S is the entropy), for each phase (solid, liquid) to be decomposed into a cold (T -independent) piece, an ionic excitation term, and an electronic excitation term,

$$F(\rho, T) = E_{\text{cold}}(\rho) + F_{\text{ion}}(\rho, T) + F_{\text{electron}}(\rho, T). \quad (6)$$

For the cold term, we use a Vinet-Rose analytic form in the neighborhood of ambient density [58], which is then joined through spline interpolation to a higher-density form derived from the results of DFT calculations. Note that we use the construct of a cold piece even for the liquid, although this phase is not thermodynamically favored at low T . For the ionic excitation term, we employ a Debye model with phase-dependent and density-dependent Debye

temperature $\theta(\rho)$,

$$F_{\text{Debye}}(\rho, T) = k_{\text{B}}T \left[\frac{9}{8} \frac{\theta(\rho)}{T} + 3 \ln\{1 - \exp[-\theta(\rho)/T]\} + D[\theta(\rho)/T] \right], \quad (7)$$

where

$$D[y] = \frac{3}{y^3} \int_0^y \frac{x^3}{e^x - 1} dx. \quad (8)$$

Since the first term, equal to $9/8k_{\text{B}} \times \theta$ and arising from quantum zero-point motion, is independent of T , we subsume it into $E_{\text{cold}}(\rho)$ and assign the remainder to the ionic excitation term,

$$F_{\text{ion}}(\rho, T) = F_{\text{Debye}}(\rho, T) - \frac{9}{8}k_{\text{B}}\theta(\rho). \quad (9)$$

We take the electronic excitation component from a DFT spherical atom-in-jellium model known as Purgatorio [59], which is an update of the earlier Inferno [60] model. This neglects the directionality of chemical bonding but includes electronic ionization (due to both temperature and pressure) in detail. As in Ref. [57], we use this contribution for *both* solid and liquid phases of Ta, where the $T = 0$ Purgatorio bonding contribution yields the contribution to electronic excitations, specifically,

$$F_{\text{electron}}(\rho, T) = F_{\text{Purgatorio}}(\rho, T) - F_{\text{Purgatorio}}(\rho, T = 0). \quad (10)$$

We also add our cell model contribution [61] to the ion-thermal term for the liquid phase; this ensures that $\lim_{T \rightarrow \infty} E_{\text{ion}}(\rho, T) = \frac{3}{2}k_{\text{B}}T$ per ion and $\lim_{T \rightarrow \infty} P_{\text{ion}}(\rho, T) = k_{\text{B}}T\rho/m_{\text{ion}}$, as required for the ideal gas EOS to be reached (although we mention this addition for completeness, it is of negligible import for the fitting to the DAC, shock, and ramp compression data of primary concern in this work).

B. Model fitting and validation

Given that our choice of F_{electron} is fixed by simulations, our fitting of the EOS model for Ta involves the specification of four ρ -dependent functions: $E_{\text{cold}}^{\text{solid}}(\rho)$, $\theta^{\text{solid}}(\rho)$, $E_{\text{cold}}^{\text{liquid}}(\rho)$, and $\theta^{\text{liquid}}(\rho)$, where $E_{\text{cold}}^{\text{liquid}}(\rho) - E_{\text{cold}}^{\text{solid}}(\rho)$ is the major contributor to the solid-liquid internal energy difference and $\theta^{\text{solid}}(\rho)/\theta^{\text{liquid}}(\rho)$ is the major contributor to the entropy difference. Our strategy is to use DAC isotherm measurements and this work's ramp compression data (see the solid black curve in Fig. 4) to constrain $P_{\text{cold}}^{\text{solid}}(\rho)$ ($= \frac{\rho^2}{m_{\text{Ta}}} \frac{dE_{\text{cold}}^{\text{solid}}}{d\rho}$, shown as the cyan curve in Fig. 4) and experimental measurements of the following quantities to constrain the functions $E_{\text{cold}}^{\text{liquid}}(\rho)$, $\theta^{\text{solid}}(\rho)$, and $\theta^{\text{liquid}}(\rho)$: (1) ambient pressure thermal expansion, (2) ambient pressure entropy, (3) $T_{\text{melt}}(\rho)$, (4) shock Hugoniot $P(\rho)$, and (5) pressures of the intersection between the Hugoniot and the melt curve. In addition to these constraining data, we augment them with DFT molecular dynamics (MD) inferences of the solid entropy along two isochores ($\rho = 16.7025 \text{ g/cm}^3$ and 30.5927 g/cm^3). The

fitting procedure we use is an iterative one, where $E_{\text{cold}}^{\text{solid}}(\rho)$, $\theta^{\text{solid}}(\rho)$, $E_{\text{cold}}^{\text{liquid}}(\rho)$, and $\theta^{\text{liquid}}(\rho)$ are varied in concert until a satisfactory agreement with all data is obtained. This is aided by our use of the MEOS multiphase equation of state generation code [57].

In practice, the $\theta(\rho)$ functions are determined by first constraining them at low ρ from the ambient pressure entropy (inferred from specific heat data), and then their elevated- ρ behavior is extracted by inverting the relationship:

$$\gamma_{\text{ion}}(\rho) = \frac{\rho}{\theta(\rho)} \frac{d\theta}{d\rho}, \quad (11)$$

where γ_{ion} is the ionic Grüneisen parameter, which itself is extracted from the high- T ($T > \theta$) behavior of the ionic pressure,

$$P_{\text{ion}}(\rho, T > \theta) = \frac{C_{\text{V}}T}{V} \gamma_{\text{ion}}(\rho), \quad (12)$$

where V ($= m_{\text{Ta}}/\rho$) is the atomic volume and C_{V} is the constant-volume specific heat. Our values for P_{ion} are culled from the total thermal contribution, after subtracting the electronic contribution to the pressure resulting from Eq. (10). The total thermal contribution (ionic + electronic) to the pressure is obtained from $P_{\text{total}} - P_{\text{cold}}$; indeed, it is here that the inclusion of our ramp compression data is crucial, as it provides a tight constraint on $P_{\text{cold}}(\rho)$ throughout the full range of ρ where $P_{\text{total}}^{\text{Hugoniot}}(\rho)$ is obtainable from shock data.

Figure 5(a) shows our fit to the ambient pressure thermal expansion data of Touloukian *et al.* for the solid phase [62]. Figure 5(b) displays agreement between our Ta EOS and DFT-MD calculations of the total entropy of solid Ta along the isochore $\rho = 30.5927 \text{ g/cm}^3$. Here, the DFT-MD entropy predictions were made by us using a procedure akin to that presented in the work of Teweldeberhan *et al.* [64]. This agreement ensures that our choice of $\theta^{\text{solid}}(\rho)$ at these densities is reasonable. We deem this to be particularly important since entropy at elevated pressures is a quantity which is still unconstrained by direct experimental measurement. We also ensured agreement with our lower- ρ DFT-MD entropy isochore at 16.7025 g/cm^3 . Figure 5(c) shows a large collection of $P(\rho)$ principal shock Hugoniot data, along with the principal Hugoniot of our EOS model (also shown in Fig. 4 by gray triangles and the gray curve). Agreement with these data was affected by choosing $\gamma_{\text{ion}}(\rho)$ [see Eqs. (9), (11), and (12)] once $E_{\text{cold}}(\rho)$ had been constrained by a combination of DAC isotherm data and the NIF ramp compression measurements presented above. Figure 5(d) presents comparisons between our EOS model and experimental data of pressure vs particle velocity for (assumed adiabatic) releases from various shock states. Here, the solid black line is the principal Hugoniot of our EOS model, and the colored dashed lines represent our model's isentropes launched from various Hugoniot states. Note the excellent agreement throughout, suggesting that our high- T , low- ρ liquid free energy model is accurate in this regime. This lends further credence to our choice of $\gamma_{\text{ion}}^{\text{liquid}}(\rho)$ at low ρ .

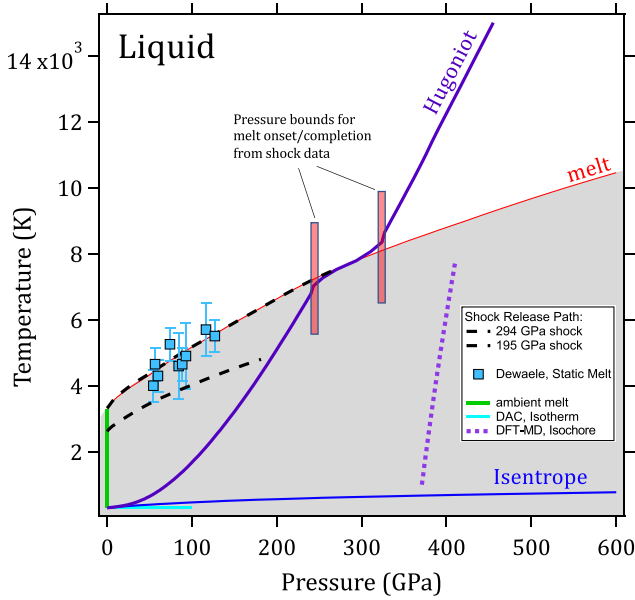


FIG. 6. Temperature-pressure phase diagram of Ta which shows the experimental constraints used in the construction of the high- T EOS. Ramp compression (blue line) and 300 K DAC [52] (cyan line) data provide constraints on $P_{\text{cold}}(\rho)$. Existing ambient pressure heating [62] (green line), laser-heated DAC [65] (cyan squares), Hugoniot (purple line), and shock melting [19] (red bars) data are used to constrain $P_{\text{thermal}}(\rho, T)$. Comparisons with isochores calculated at high pressure using DFT-based molecular dynamics (purple dotted line) and release isentropes measured from plate impact experiments [63] (black dashed line) provide scrutiny of the performance of the EOS.

Figure 6 shows an illustration of tantalum's T vs P phase diagram once again, but now with the locations of the various experimental and *ab initio* theoretical constraints superposed. We note here that unlike for the other constraints, the principal Hugoniot constraint (red curve) is really a constraint of P vs ρ ; the temperature (y axis) of the red curve in Fig. 6 is a *prediction* of our EOS model. Nevertheless, our match to the pressures of the intersection between the Hugoniot and T_{melt} (shown as the red vertical bars) is key to our determination of the latent heat of melting (involving both the solid-liquid internal energy difference and the entropy difference) assumed within our Ta EOS model.

IV. DISCUSSION

There have been several previous attempts to construct a high- T EOS of Ta using classical molecular dynamics [66], first-principles molecular dynamics [10–12], and also semi-empirical methods, as in this work. However, these previous studies were all limited in pressure to between 0.1 and 0.3 TPa as they relied on previous DAC data to anchor $P_{\text{cold}}(\rho)$. Along a 3000 K isotherm, the pressure disagreement between previous models is already as high as $\sim 10\%$ at 0.25 TPa (Fig. S8 [28]) and continues to diverge at higher pressures. Our EOS is experimentally constrained and accurate up to pressures and temperatures far beyond the stated applicability limits of these previous models (Figs. 1 and S8 [28]) due to its enforced

TABLE I. Best-fit parameters for a third-order Vinet fit to the calculated isotherms at 298, 1000, 2000, 3000, 4000, and 5000 K from our high- T EOS of tantalum. The initial densities for each isotherm were taken to be 16.650, 16.444, 16.038, 15.415, 14.778, and 13.503 g/cm³, respectively.

T (K)	K_0 (GPa)	η	β	Ψ
298	179.60(2.18)	4.68(0.16)	-0.22(0.72)	10.08(1.03)
1000	175.9(2.21)	4.46(0.17)	0.72(0.73)	8.79(1.04)
2000	161.88(2.06)	4.42(0.17)	1.24(0.72)	7.76(1.00)
3000	128.67(1.81)	5.46(0.18)	-2.20(0.73)	11.75(0.98)
4000	104.00(1.71)	6.13(0.20)	-4.00(0.79)	13.41(1.02)
5000	51.86(1.26)	9.69(0.27)	-14.30(1.00)	23.66(1.20)

agreement with the ramp compression measurements up to 2.3 TPa.

This significant advancement in high- T EOS development, brought about by laser-driven ramp compression, coincides with a recent experimental breakthrough in static compression, where laser heating techniques were successfully coupled with a DSDAC, allowing sample conditions beyond 1 TPa and ~ 3000 K to be accessed [4]. In such experiments, x-ray diffraction is used to determine the sample density under compression, while pyrometric techniques are used to estimate sample temperature [67]. The ability to access such extreme conditions is promising for novel material syntheses as the first results from such experiments have demonstrated the recovery of new rhenium alloys [4]. In planetary science, the potential surface habitability of newly discovered rocky exoplanets is dependent on planetary interior conditions which, for example, on Earth result in tectonic activity, surface outgassing, and the production of a magnetosphere. These extreme interior states of matter can now be investigated through high-pressure, high-temperature experiments where the composition and crystal structure of core-mantle constituents are predicted to transform above ~ 1 TPa and 4000 K for a 10 Earth mass rocky exoplanet [68] (Fig. 1).

Our wider-range Ta EOS model renders this material the only one with a P - ρ - T EOS which is well constrained at the conditions relevant to these new physics frontiers which are now accessible by coupling laser heating to DSDAC compression. By its inclusion in the sample chamber, Ta could be used as a high-temperature pressure standard where the Ta pressure state, assumed to be in equilibrium with the sample of interest, can be determined directly from the diffraction data at a known temperature. The chemical reaction between the sample, standard, and diamonds [65] can be minimized with the use of single-pulse laser heating setups [69] that have submillisecond heating pulse durations.

Accordingly, we have fitted several isotherms from our model to a Vinet EOS and provide the fitting parameters for the 298, 1000, 2000, 3000, 4000, and 5000 K isotherms in Table I. The form of the Vinet fitting follows Refs. [16,49,50,70] and is $P(X) = 3K_0[(1 - X^{1/3})/X^{2/3}] \exp[\eta(1 - X^{1/3}) + \beta(1 - X^{1/3})^2 + \Psi(1 - X^{1/3})^3]$, where $X = \rho/\rho_0$, K_0 is the bulk modulus, and η , β , and Ψ are other fitting parameters. We recommend using our isotherms up to 2.3 TPa and 5000 K.

V. CONCLUSION

In conclusion, we have measured the isentropic compression of tantalum to 2.3 TPa. From this, we have constructed an experimentally constrained high- T EOS for tantalum up to multiterapascal pressures and several thousand degrees Kelvin, which will serve as a means to determine pressure at extreme compressions and elevated temperatures now achievable using laser-heated DSDACs. While Ta may be a promising high- T pressure standard, our work represents a general method for high- T EOS construction. Ramp compression experiments have also been performed on other materials to multiterapascal pressures [14,16,17], providing a road map for building an accurate high- T EOS catalog at extreme conditions.

ACKNOWLEDGMENTS

We thank the laser and target fabrication staff of the NIF. This work was performed under the auspices of the U.S. Department of Energy by Lawrence Livermore National Laboratory under Contract No. DE-AC52-07NA27344.

-
- [1] A. Friedrich, B. Winkler, L. Bayarjargal, W. Morgenroth, E. A. Juarez-Arellano, V. Milman, K. Refson, M. Kunz, and K. Chen, *Phys. Rev. Lett.* **105**, 085504 (2010).
- [2] E. Gregoryanz, C. Sanloup, M. Somayazulu, J. Badro, G. Fiquet, H.-k. Mao, and R. J. Hemley, *Nat. Mater.* **3**, 294 (2004).
- [3] S. Anzellini, A. Dewaele, M. Mezouar, P. Loubeyre, and G. Morard, *Science* **340**, 464 (2013).
- [4] L. Dubrovinsky, S. Khandarkhaeva, T. Fedotenko, D. Laniel, M. Bykov, C. Giacobbe, E. Lawrence Bright, P. Sedmak, S. Chariton, V. Prakapenka, A. V. Ponomareva, E. A. Smirnova, M. P. Belov, F. Tasnádi, N. Shulumba, F. Trybel, I. A. Abrikosov, and N. Dubrovinskaia, *Nature (London)* **605**, 274 (2022).
- [5] R. Briggs, F. Coppari, M. G. Gorman, R. F. Smith, S. J. Tracy, A. L. Coleman, A. Fernandez-Pañella, M. Millot, J. H. Eggert, and D. E. Fratanduono, *Phys. Rev. Lett.* **123**, 045701 (2019).
- [6] S. M. Sharma, S. J. Turneaure, J. M. Winey, and Y. M. Gupta, *Phys. Rev. B* **102**, 020103(R) (2020).
- [7] S. M. Sharma, S. J. Turneaure, J. M. Winey, and Y. M. Gupta, *Phys. Rev. Lett.* **124**, 235701 (2020).
- [8] S. K. Han, R. F. Smith, D. Kim, J. K. Wicks, J. R. Rygg, A. Lazicki, J. H. Eggert, and T. S. Duffy, *Phys. Rev. B* **103**, 184109 (2021).
- [9] M. Sims, R. Briggs, T. J. Volz, S. Singh, S. Hamel, A. L. Coleman, F. Coppari, D. J. Erskine, M. G. Gorman, B. Sadigh, J. Belof, J. H. Eggert, R. F. Smith, and J. K. Wicks, *J. Appl. Phys.* **132**, 075902 (2022).
- [10] S. Ono, *Int. J. Mol. Sci.* **10**, 4342 (2009).
- [11] R. E. Cohen and O. Gülseren, *Phys. Rev. B* **63**, 224101 (2001).
- [12] S. Taioli, C. Cazorla, M. J. Gillan, and D. Alfè, *J. Phys.: Conf. Ser.* **121**, 012010 (2008).
- [13] P. I. Dorogokupets and A. R. Oganov, *Phys. Rev. B* **75**, 024115 (2007).
- [14] R. F. Smith, D. E. Fratanduono, D. G. Braun, T. S. Duffy, J. K. Wicks, P. M. Celliers, S. J. Ali, A. Fernandez-Pañella, R. G. Kraus, D. C. Swift, G. W. Collins, and J. H. Eggert, *Nat. Astron.* **2**, 452 (2018).
- [15] N. Nettelmann, R. Helled, J. Fortney, and R. Redmer, *Planet. Space Sci.* **77**, 143 (2013).
- [16] D. E. Fratanduono, R. F. Smith, S. J. Ali, D. G. Braun, A. Fernandez-Pañella, S. Zhang, R. G. Kraus, F. Coppari, J. M. McNaney, M. C. Marshall, L. E. Kirch, D. C. Swift, M. Millot, J. K. Wicks, and J. H. Eggert, *Phys. Rev. Lett.* **124**, 015701 (2020).
- [17] D. E. Fratanduono, M. Millot, D. G. Braun, S. J. Ali, A. Fernandez-Pañella, C. T. Seagle, J.-P. Davis, J. L. Brown, Y. Akahama, R. G. Kraus, M. C. Marshall, R. F. Smith, E. F. O'Bannon, J. M. McNaney, and J. H. Eggert, *Science* **372**, 1063 (2021).
- [18] D. Orlikowski, P. Söderlind, and J. A. Moriarty, *Phys. Rev. B* **74**, 054109 (2006).
- [19] R. G. Kraus, F. Coppari, D. E. Fratanduono, R. F. Smith, A. Lazicki, C. Wehrenberg, J. H. Eggert, J. R. Rygg, and G. W. Collins, *Phys. Rev. Lett.* **126**, 255701 (2021).
- [20] L. V. Al'tshuler, A. A. Bakanova, I. P. Dudoladov, E. A. Dynin, R. F. Trunin, and B. S. Chekin, *J. Appl. Mech. Tech. Phys.* **22**, 145 (1981).
- [21] R. G. McQueen, S. P. Marsh, J. W. Taylor, J. N. Fritz, and W. J. Carter, in *High-Velocity Impact Phenomena*, edited by R. Kinslow (Academic Press, New York, 1970), Chap. 12.
- [22] S. P. Marsh, in *LASL Shock Hugoniot Data*, edited by S. P. Marsh (University of California Press, Berkeley, 1980), p. 136.
- [23] A. C. Mitchell and W. J. Nellis, *J. Appl. Phys.* **52**, 3363 (1981).
- [24] N. C. Holmes, J. A. Moriarty, G. R. Gathers, and W. J. Nellis, *J. Appl. Phys.* **66**, 2962 (1989).
- [25] R. F. Trunin, N. V. Panov, and A. B. Medvedev, *Pis'ma Zh. Eksp. Teor. Fiz.* **62**, 572 (1995).
- [26] G. R. Gathers, *Int. J. Thermophys.* **4**, 149 (1983).
- [27] M. Matsui, *J. Phys.: Conf. Ser.* **215**, 012197 (2010).
- [28] See Supplemental Material at <http://link.aps.org/supplemental/10.1103/PhysRevB.107.014109> for additional information on experimental methods and model assumptions as well as tabular data.
- [29] R. Fowles and R. F. Williams, *J. Appl. Phys.* **41**, 360 (1970).
- [30] D. L. Preston, D. L. Tonks, and D. C. Wallace, *J. Appl. Phys.* **93**, 211 (2003).
- [31] N. R. Barton and M. Rhee, *J. Appl. Phys.* **114**, 123507 (2013).
- [32] C. Perreault, L. Q. Huston, K. Burrage, S. C. Couper, L. Miyagi, E. K. Moss, J. S. Pigott, J. S. Smith, N. Velisavljevic, Y. Vohra, and B. T. Sturtevant, *J. Appl. Phys.* **131**, 015905 (2022).
- [33] P. S. Follansbee and U. F. Kocks, *Acta Metall.* **36**, 81 (1988).
- [34] D. C. Swift, K. Alidoost, R. Austin, T. Lockard, C. Wu, S. Hamel, J. E. Klepeis, and P. Peralta, [arXiv:2110.06345](https://arxiv.org/abs/2110.06345).
- [35] F. Birch, *J. Appl. Phys.* **9**, 279 (1938).
- [36] P. Vinet, J. H. Rose, J. Ferrante, and J. R. Smith, *J. Phys.: Condens. Matter* **1**, 1941 (1989).
- [37] A. Berthault, L. Arles, and J. Matricon, *Int. J. Thermophys.* **7**, 167 (1986).
- [38] E. S. Domalski and E. D. Hearing, Condensed phase heat capacity data, in *NIST Chemistry WebBook*, edited by P. J. Linstrom and W. G. Mallard, NIST Standard Reference Database No.

- 69 (NIST, Gaithersburg, MD, 2018), <https://webbook.nist.gov/chemistry>.
- [39] J. M. Wills, M. Alouani, P. Andersson, A. Delin, O. Eriksson, and O. Grechnev, *Full-Potential Electronic Structure Method: Energy and Force Calculations with Density Functional and Dynamical Mean Field Theory*, Springer Series in Solid-State Sciences, Vol. 167 (Springer-Verlag, Berlin, 2010).
- [40] L. Nordström, J. Wills, P. H. Andersson, P. Söderlind, and O. Eriksson, *Phys. Rev. B* **63**, 035103 (2000).
- [41] J. Eggert, R. Smith, D. Swift, R. Rudd, D. Fratanduono, D. Braun, J. Hawrelak, J. McNaney, and G. Collins, *High Pressure Res.* **35**, 339 (2015).
- [42] P. M. Celliers, D. K. Bradley, G. W. Collins, D. G. Hicks, T. R. Boehly, and W. J. Armstrong, *Rev. Sci. Instrum.* **75**, 4916 (2004).
- [43] D. C. Swift, D. E. Fratanduono, R. G. Kraus, and E. A. Dowling, *Rev. Sci. Instrum.* **90**, 093903 (2019).
- [44] C. W. Greeff and J. D. Johnson, *New Sesame Equation of State for Tantalum*, Technical Report LA-13681-MS (Los Alamos National Laboratory, Los Alamos, NM, 2000).
- [45] C. Kittel and H. Kroemer, *Thermal Physics* (Wiley, New York, 1970), Vol. 9690.
- [46] D. Rittel, A. Bhattacharyya, B. Poon, J. Zhao, and G. Ravichandran, *Mater. Sci. Eng., A* **447**, 65 (2007).
- [47] J.-P. Davis, J. L. Brown, M. D. Knudson, and R. W. Lemke, *J. Appl. Phys.* **116**, 204903 (2014).
- [48] J. L. Brown, J.-P. Davis, and C. T. Seagle, *J. Dyn. Behav. Mater.* **7**, 196 (2021).
- [49] Y. Wang, R. Ahuja, and B. Johansson, *J. Appl. Phys.* **92**, 6616 (2002).
- [50] A. D. Chijioke, W. J. Nellis, and I. F. Silvera, *J. Appl. Phys.* **98**, 073526 (2005).
- [51] H. Cynn and C.-S. Yoo, *Phys. Rev. B* **59**, 8526 (1999).
- [52] A. Dewaele, P. Loubeyre, and M. Mezouar, *Phys. Rev. B* **69**, 092106 (2004).
- [53] K. C. Burrage, C. S. Perreault, E. K. Moss, J. S. Pigott, B. T. Sturtevant, J. S. Smith, N. Velisavljevic, and Y. K. Vohra, *High Pressure Res.* **39**, 489 (2019).
- [54] K. W. Katahara, M. H. Manghnani, and E. S. Fisher, *J. Appl. Phys.* **47**, 434 (1976).
- [55] M. Hanfland, K. Syassen, and J. Köhler, *J. Appl. Phys.* **91**, 4143 (2002).
- [56] D. L. Heinz and R. Jeanloz, *J. Appl. Phys.* **55**, 885 (1984).
- [57] C. J. Wu, P. C. Myint, J. E. Pask, C. J. Prisbrey, A. A. Correa, P. Suryanarayana, and J. B. Varley, *J. Phys. Chem. A* **125**, 1610 (2021).
- [58] P. Vinet, J. Ferrante, J. H. Rose, and J. R. Smith, *J. Geophys. Res.* **92**, 9319 (1987).
- [59] B. Wilson, V. Sonnad, P. Sterne, and W. Isaacs, *J. Quant. Spectrosc. Radiat. Transfer* **99**, 658 (2006).
- [60] D. A. Liberman, *Phys. Rev. B* **20**, 4981 (1979).
- [61] L. X. Benedict, K. P. Driver, S. Hamel, B. Militzer, T. Qi, A. A. Correa, A. Saul, and E. Schwegler, *Phys. Rev. B* **89**, 224109 (2014).
- [62] Y. S. Touloukian, R. W. Powell, C. Y. Ho, and M. C. Nicolaou, *Thermophysical Properties of Matter—The TPRC Data Series, Thermal Diffusivity* (Thermophysical and Electronic Properties Information Analysis Center, Lafayette, 1974), Vol. 10.
- [63] W. Nellis, A. Mitchell, and D. Young, *J. Appl. Phys.* **93**, 304 (2003).
- [64] A. M. Teweldeberhan, J. L. Dubois, and S. A. Bonev, *Phys. Rev. Lett.* **105**, 235503 (2010).
- [65] A. Dewaele, M. Mezouar, N. Guignot, and P. Loubeyre, *Phys. Rev. Lett.* **104**, 255701 (2010).
- [66] Z.-L. Liu, X.-L. Zhang, L.-C. Cai, X.-R. Chen, Q. Wu, and F.-Q. Jing, *J. Phys. Chem. Solids* **69**, 2833 (2008).
- [67] S. Anzellini and S. Boccato, *Crystals* **10**, 459 (2020).
- [68] T. S. Duffy and R. F. Smith, *Front. Earth Sci.* **7**, 23 (2019).
- [69] Z. Konôpková, W. Morgenroth, R. Husband, N. Giordano, A. Pakhomova, O. Gutowski, M. Wendt, K. Glazyrin, A. Ehnes, J. T. Delitz, A. F. Goncharov, V. B. Prakapenka, and H.-P. Liermann, *J. Synchrotron Radiat.* **28**, 1747 (2021).
- [70] R. G. Kraus, J.-P. Davis, C. T. Seagle, D. E. Fratanduono, D. C. Swift, J. L. Brown, and J. H. Eggert, *Phys. Rev. B* **93**, 134105 (2016).